Research paper

The influence of printing parameters on multi-material two-photon polymerisation based micro additive manufacturing

Qin Hu [a], Graham A. Rance [b], Gustavo F. Trindade [a,c], David Pervan [a], Long Jiang [c], Aleksandra Foerster [a], Lyudmila Turyanska [a,*], Christopher Tuck [a], Derek J. Irvine [a], Richard Hague [a], Ricky D. Wildman [a,*]

[a] Faculty of Engineering, University of Nottingham, Nottingham, United Kingdom NG7 2RD
[b] Nanoscale and Microscale Research Centre, University of Nottingham, Nottingham, United Kingdom NG7 2RD
[c] School of Pharmacy, University of Nottingham, Nottingham, United Kingdom NG7 2RD

A B S T R A C T

Two-photon polymerisation (2PP) based additive manufacturing has emerged as a powerful technology to fabricate complex three-dimensional micro- and nanoscale architectures. However, a comprehensive understanding of the effect of printing parameters on the functional properties of these structures is needed to unleash the potential of 2PP and enable controlled deposition / integration of various materials into multi-material structures. In this study we investigate the correlation between printing parameters, resin composition and the final properties of 2PP structures fabricated with different monomers and initiators. The link between 2PP process and final material properties is validated by morphological studies, vibrational spectroscopy and advanced mass spectrometry, ToF-SIMS, imaging. We establish empirical relationships between printing parameters and mechanical properties, and achieve controlled deposition of different monomers with high precision and uniform composition. The approaches developed here are successfully used to demonstrate multi-material 2PP and produce complex 3D architectures incorporating three polymers. The 2PP structures produced can be transferred into solution or onto different substrates, in addition to direct fabrication on flexible substrates. This work advances the understanding of the 2PP process, which enable rational design and manufacture of complex geometries and additive manufacturing of nanoscale multi-material structures.

1. Introduction

Two-photon polymerisation (2PP) based micro/nano additive manufacturing is a powerful technology to fabricate complex three-dimensional (3D) micro/nano architectures, without the need for a mask, in a fast and controllable fashion [1–4]. The overall size can be scaled up to the centimetre range, but retains a resolution close to 100 nm. A range of polymers, hydrogels, nanomaterials and biomaterials can be processed with this approach. The flexibility offered by 2PP for architecting design and material selection opens up new opportunities for manufacturing functional devices. This has been achieved by the development of functional resins, which enable the tailoring of mechanical, optical, electrical and magnetic properties of final structures [1], by in-flow growth of nanomaterials [2,3] and by post-deposition functionalization of printed structures with nanomaterials, e.g. gold

nano-islands [4]. Consequently, the flexibility offered by 2PP materials and architected designs is beneficial across a range of applications, from optoelectronics [5] to the biomedical sector [6].

2PP is a growing technological area but is yet to fully unleash its potential; as such, a comprehensive understanding of how the printing parameters impact upon the polymerization process is required. The specific choice of initiator is important in this respect and a number of novel 2PP initiators have been used recently to both achieve enhanced two-photon activity [2,7] and/or manipulate the final properties of the printed structures [8,9]. Optimization of the printing parameters and deposition strategy provides additional control of material properties and is of key importance in achieving control of functionality. For example, colour printing was demonstrated using the shrinking of photonic crystals [10] and parameter optimization enabled printing of retinal cell grafts [11]. Yet, one of the main factors holding back the

advancement of 2PP is the inability to produce components from a wider range of materials. Understanding and optimising the photoinitiator performance with various different monomers remains challenging, and has a crucial influence on the properties of final solid structures. Typically, to minimise biotoxicity and colour change the quantity of photoinitiator used should be limited. However, where this is not possible, a modified printing strategy is required to ensure part integrity, whilst minimising the amount of laser processing. Developing the detailed in-depth understanding of the complex properties of 2PP structures fabricated using different monomer-photoinitiator pairs is paramount for their technological advancement and could enable deposition of multimaterial structures with well-defined geometries on the micro- and nano-scale. While continuous efforts are being invested into investigation of multiphoton process [12–14], fabrication of multi-material structures is yet to be fully explored and could offer exciting opportunities for their applications as multifunctional drug delivery vehicles, metamaterials and photonic materials with response tailored by geometry.

In this study, we probed the effect of the printing parameters, resin composition and post-processing treatment on the final material properties of 2PP structures fabricated from a number of different monomers. The correlations between resin formulation (monomer-initiator pairs), laser power, scanning speed, hatching / slicing distances, and resolution and properties of the 2PP structures is explored. We establish an empirical relationship that allows the prediction of the mechanical properties of the 2PP structures from the assigned printing parameters. By optimising both the printing strategy and post-deposition processing, we produce complex architectures with uniform composition, as demonstrated by morphological (AFM and SEM) and advanced compositional studies (Raman spectroscopy and ToF-SIMS). Furthermore, the printing strategies developed for individual monomers enabled a high degree of fabrication freedom: e.g. they allowed fabrication of structures on flexible substrates, transfer of 2PP structures into solution or onto a different substrate and fabrication of multimaterial structures. Thus, we successfully demonstrate the potential scope of high-resolution multi-material 2PP of complex architectures. This work is relevant for the development of controlled deposition of materials at nano- and micro-scale length scales and their integration into multi-material structures, for applications ranging from photonics to medical devices.

2. Materials and methods

2.1. Materials

Monomers and initiators were purchased and used without further purification. Monomers used are Pentaerythritol triacrylate (PETA), (bisphenol A ethoxylate diacrylate (BPEDA), trimethylolpropane ethoxylate triacrylate (TMPETA), and poly(ethylene glycol) diacrylate (PEGDA)).

Initiators used include 7-diethylamino-3-thenoylcoumarin (DETC), 2,4-diethyl-9H-thioxanthen-9-one (DETX), 2-benzyl-2-(dimethylamino)-4′-morpholinobutyrophenone (Irgacure 369), Phenylbis-(2,4,6-trimethylbenzoyl)-phosphine oxide (Irgacure 819), and ethyl-4-(dimethylamino)-benzoate (EDB) (see Supplementary Information, SI1).

2.2. Two photon polymerization

A Commercial two-photon lithography system was used to fabricate 3D microstructures. A Nanoscribe Photonic Professional GT (Nanoscribe), equipped with a fiber-couple diode laser at a wavelength of 780 nm, pulse frequency of 80 MHz and pulse duration of 120 fs. An oil immersion objective (63x, NA = 1.4, WD = 190 μm) was used to focus the laser beam. The full power of the system was 50 mW. Micro/nano 3D structures were formed by moving the laser beam in X-Y directions using a galvo-scanner and moving a piezo stage in the Z direction accordingly.

Following laser exposure, the samples were soaked in propylene glycol monomethyl ether acetate (PGMEA) for 15 min, then washed with 2-propanol for 2 min to remove residual resin. The sample was dried under a flow of nitrogen gas. Both the resin preparation and two-photon fabrication were carried out in UV-free environment.

2.3. Raman spectroscopy

Micro Raman spectroscopy was performed using a Horiba Jobin Yvon LabRAM HR equipped with an automated *xyz* stage (Märzhäuser). Excitation was provided by a laser line at $\lambda = 660$ nm ($P = 9$ mW) or $\lambda = 785$ nm $P = 24$ mW). A 100x objective lens and a confocal pinhole of 50 μm was used. To simultaneously scan a range of Raman shifts, a 600 lines mm^{-1} rotatable diffraction grating along a path length of 800 mm was employed. Spectra were acquired using a Synapse CCD detector (1024 pixels) thermoelectrically cooled to -60 °C. Before spectra collection, the instrument was calibrated using the zero-order line at 0 nm and a standard Si(100) reference band at 520.7 cm^{-1}. For single point measurements, spectra were acquired over the range 1500–1850 cm^{-1} with an acquisition time of 120–300 s and 8–16 accumulations. The spectral resolution is 1.0 and 0.6 cm^{-1} for the 660 and 785 nm lasers, respectively, under these conditions. The spatial resolution is ~1 μm and ~3 μm in the lateral (*xy*) and axial (*z*) directions, respectively. Spectra were baseline-corrected using a fourth-order polynomial fitting model. The proportion of vinyl groups consumed, degree of consumption (*DC*), was calculated using:

$$DC = \left[1 - \left(\frac{A_{C=C}/A_{C=O}}{A'_{C=C}/A'_{C=O}}\right)\right] \times 100 \qquad (1)$$

where $A_{C=C}$, $A_{C=O}$ and $A'_{C=C}$, $A'_{C=O}$ are the integrated peak intensities in the polymerised structures and the non-polymerised liquid resin, respectively, corresponding to C=C stretching (~1570–1680 cm^{-1}) and C=O stretching (1680–1780 cm^{-1}) vibrational modes. Spectroscopic maps were recorded at 2 μm steps within a square 24 × 24 μm. Each spectrum was collected for 90 s. The ratio in Eq. (1) was evaluated using univariate analysis.

2.4. Morphological characterization

Surface morphology was characterised by scanning electron microscopy (SEM) (Hitachi TM3030) and atomic force microscopy (AFM) (Dimension Icon, Bruker Instrument). AFM imaging work was carried out in PeakForce tapping mode using RTESPA 150 (Bruker) tips. Samples were examined with a scan size of 5 μm × 5 μm.

AFM data analysis was performed using NanoScope Analysis 1.9 software (Bruker).

2.5. ToF-SIMS

ToF-SIMS mapping of 2PP shapes was carried out using a 3D Orbi-SIMS (Hybrid SIMS) instrument from IONTOF GmbH. The ToF-SIMS data were acquired in positive ion polarity mode in delayed extraction mode by raster scanning a 30 keV Bi$_3^+$ primary ion beam delivering 0.08 pA and a low-energy (20 eV) electron flood gun employed to neutralise charge build up. The section of the hollow sphere was produced by irradiating the sample with an argon gas cluster ion beam (GCIB) operated with 20 keV and 2000 atoms in the cluster with 5 nA beam current. Multivariate analysis was carried out using the mass as the variables and mapping pixels as observations. For each dataset, Surface Lab 7.1 (IONTOF GmbH) was used to perform an automated peak search on the total spectra restricted only to peaks with intensity higher than 50 counts and *m/z* between 2 u and 300 u. Dead-time corrected peak areas were then exported for each pixel. Principal component analysis (PCA) was performed using the simsMVA software [15].

2.6. Young modulus and hardness measurements

Young's modulus and hardness was characterised by nano-indentation (Micro Materials NanoTest P3). The Young modulus, E, was calculated followed the standard ISO 14577, where E is calculated from the slope of the tangent of the elastic unloading response, S, and the area function, A, using the expression: $E = \sqrt{\pi}S/2\sqrt{A}$. Three sets of samples were produced with varying hatching ($h = 0.3$, 0.5 and 0.7) and slicing (from $s = 0.1–1$) distances. To minimize effect of environmental perturbations, the machine is located inside a polymethyl methacrylate (PMMA) enclosure. A Berkovich indenter ($\theta = 65.27°$) was used. During loading, dwell and unloading the load-displacement curve was recorded. The load applied was increased linearly at a rate of 0.1 mN s^{-1} up to a maximum load of 10 mN. At 10 mN the load was maintained for 180 s dwell time to allow the material to creep and the displacement was measured. The load was then decreased at a rate of 0.1 mN s^{-1}.

3. Results and discussion

The library of monomers used in 2PP is rapidly expanding, with current focus on the particular selection of monomer-initiator pairs which: (i) have suitable polymerisation rates and physical properties (both pre- and post-polymerisation), (ii) allow the fabrication of architectures with sub-micrometre feature sizes and (iii) expand the material selection for multi-material printing. A broad range of monomers and initiators were used in this work to explore the effect of monomer type and its molecular weight, as well as initiator concentration on the final properties of 2PP structures (see Supplementary Information SI1, Table S1).

A commercial two-photon lithography system, a Nanoscribe Photonic Professional GT, equipped with a fibre-coupled diode-laser ($\lambda = 780$ nm) was used to fabricate the structures. The following parameters are used in the 2PP process: laser power, P; scanning speed, v, hatching distance, h (the distance between the centres of a Gaussian laser beam in adjacent lines in the x-y plane); and slicing distance, s (the distance between the centres of the laser beam in adjacent layers in the z direction) (Supplementary Information SI1, Fig. S1). A variety of structures was produced and analysed, from printed cubes to fullerene-type architectures. SEM images of representative structures (Fig. 1a) reveal high degree of spatial control, with high resolution down to the sub-micron length scale achieved by the 2PP process. To assess the effect of printing parameters, such as initiator concentration, laser power,

hatching and slicing distance, and scan rate on the degree of monomer consumption (DC), Raman spectroscopy was used.

3.1. Monomer and initiator

PETA is a commonly used acrylate-based monomer due to its rapid polymerisation kinetics [2,10,16]. We investigated the properties of 2PP-manufactured PETA woodpile structures produced utilising one of the following initiators: DETC, DETX, Irgacure 369, Irgacure 819, EDB (see Supplementary Information, SI1). To establish the threshold concentration for each initiator, the DC values were assessed for structures produced at $P = 32.5$ mW, $v = 10$ mm/s, $h = 0.2$ μm, with varying initiator concentration. For DETC, the degree of consumption decreased from 42.8% to 33.3% as the DETC concentration decreased from 0.180 to 0.045 mol% (Fig. 1b). Whilst the DETC concentration used here is lower than that commonly reported (0.23 mol%) [17,18], the observed DC was found to be comparable to that in published literature [2,19] and approaching the maximum value of 45%, expected due to the termination of the polymerization process due to restricted oligomer mobility [19]. Further reduction of DETC concentration to ∼ 0.009 mol% resulted in significant morphological deformations of the woodpile structure attributed to a low degree of polymerization.

To achieve a $DC = 35\%$ (at $P = 32.5$ mW and $v = 10$ mm/s) with Irgacure 369, Irgacure 819 and DETX, used as alternative initiators for PETA (Fig. 1b), required 0.78, 1.25 and 1.95 mol% of initiator, respectively. These loadings were more than 10 times greater than that needed when using DETC. This difference was ascribed to slower radical generation mechanisms [20]. DETC and DETX are Type II initiators, which undergo a bimolecular process of radical generation, while Irgacure 369 and Irgacure 819 are Type I initiators, and therefore undergo a unimolecular bond cleavage. Intrinsic initiator properties, such as absorption coefficient and quantum yield for dissociation, may also play an important role in this process [21]. The DC results in Fig. 1b for DETC and DETX were obtained without a co-initiator, e.g. EDB used to improve the initiation efficiency.

With the aim of investigating the effect of reduced initiator concentration on DC, DETC was selected, and applied to three additional monomers, BPEDA, TMPETA, and PEGDA. Two molecular weight variants of each monomer were polymerised for each monomer where the M_n difference in each case was related to the length of the ethylene oxide chains within the structure, (see Fig. 1c and Supplementary Information, SI1). For all studied monomers, an increase in DC was observed with
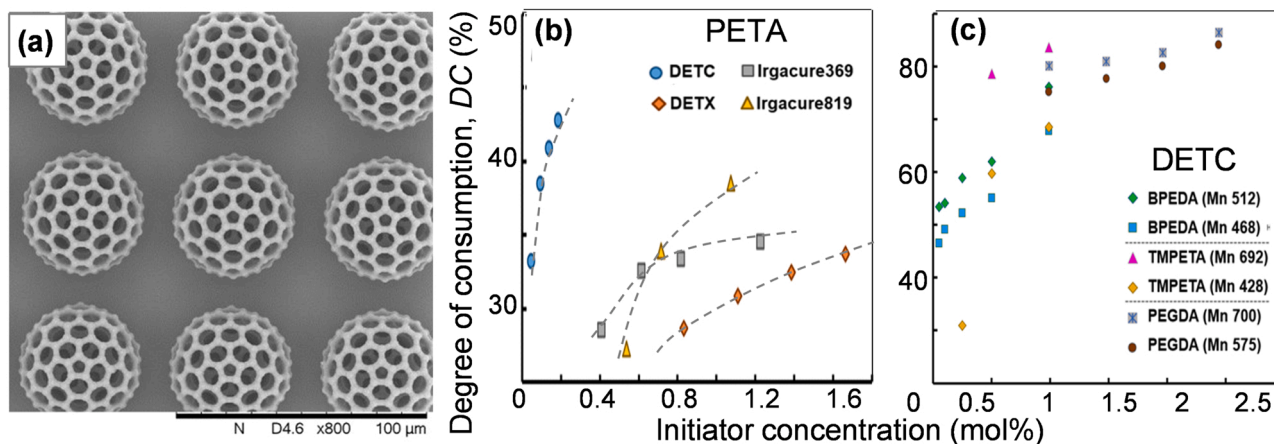

Fig. 1. (a) A representative scanning electron microscopy (SEM) image of PETA microstructures produced using 2PP additive manufacturing process. **(b)** Degree of consumption (DC) of vinyl groups in 2PP structures produced using PETA resin with the DETC, DETX, Irgacure 369 and Irgacure 819 initiators. 2PP processing parameters: laser power 32.5 mW, scan speed 10 mm/s, hatching distance 1 μm and slicing distance 0.5 μm. **(c)** Degree of consumption of vinyl groups in BPEDA, TMPETA and PEGDA monomers used with DETC initiator. All monomers are investigated with two different molecular weight (Mn). 2PP processing parameters: laser power 41.5 mW for BPEDA and TMPETA, 45 mW for PEGDA, scan speed 10 mm/s, hatching distance 1 μm and slicing distance 0.5 μm. Dashed lines are guide to an eye.

increasing DETC concentration, reaching a value of 60–80% at an initiator concentration of 0.75 mol%. The general observed trend was that a greater *DC* is achieved for larger M_n, and is likely due to smaller number of vinyl groups per unit volume, and hence a greater effective number of photons per vinyl group leading to an increased probability of successful conversion. These results demonstrate that the degree of monomer conversion is affected by the chemical structure and *Mn* of the monomer, as well as by the type and concentration of the initiator.

We examine the composition of the 2PP manufactured structures by Raman spectroscopy and ToF-SIMS imaging. Raman mapping of the surface of a 2PP cube confirmed the uniform *DC* value of 43 ± 5% (Fig. 2a). Also, post-fabrication UV exposure further increased the degree of polymerisation. For example, 30 min exposure to UV ($\lambda = 395$ nm, $P = 2$ W/cm^2) increased the vinyl group consumption by ~5% to 48 ± 5% (see Supplementary Information, SI2), exeeding the previously reported maximum value [19]. The analysis of the of the 2PP structures by ToF SIMS further confirmed the uniform composition (Fig. 2b-c and Supplementary Information, SI2). We now assess the influence of the parameters of printing process on the property of the printed architecture.

3.2. Printing parameters and scan strategy

To successfully apply 2PP commercially it is essential to understand the effect of the printing parameters on *DC* and on the functional properties of the 2PP resulting structures. The SEM images of the woodpile PETA structures with 0.18 mol% DETC and the images (Fig. 3a) clearly revealed the effect of laser power on the morphology of woodpile blocks. At low laser powers, insufficient polymerization led to undefined structures, while high laser powers result in damage associated with "burning" of the material. Based on the assessment of morphology, the effect of the laser power was qualitatively divided into five zones (Fig. 3b, scan speed 10 mm/s) where structures are: not formed, deformed (e.g. edge sagging), well-defined, with morphological defects and with significant structural damage. Thus, a laser processing window can be defined, in which structures with designed geometry were produced. It was noted that the processing window was widened with increased hatching and/or slicing distances. Interestingly, the point at which the formation of well-defined structures was observed and the threshold for laser-induced burning at higher power was reached were noted to be at lower laser powers for smaller *h* distances. This was attributed to effective laser power exposure each unit of the structure receives; thus voxel overlap at smaller *h* results in larger effective laser power exposures. Widening of the printing window was also achieved by increasing scan speed from 5 to 50 mm/s (for a hatching distance of 1 μm and slicing distance of 0.5 μm). A higher scan speed is preferred to reduce processing time and this requires monomers with fast rates of polymerisation, e.g. diacrylates and triacrylates. In this study, PETA was successfully polymerized with scan speed of up to 100 mm/s. The laser processing window also depends on the formulation. Comparing

different monomers, we find that between PEGDA (M_n 700), TCDMDA and PETA (1.7 mol% Irgacure 369, $v = 10$ mm/s, $h = 1$ μm, $s = 0.5$ μm), PETA has a relatively low threshold for polymerisation and a wider processing window.

As both laser power (Fig. 3c) and hatching distance (Fig. 3d) affect the *DC,* they correspondingly influence the physical properties of fabricated structures. When increasing laser power from 15 to 40 mW, the *DC* increased from 33% to 48%, which was accompanied by an increase of the Young's modulus, E_{PETA}, from 1.2 to 5 GPa (Fig. 3c). Increasing *h* resulted in a decrease in *DC*, reducing it to ~34%, and resulted in a corresponding decrease of E_{PETA} and hardness (Fig. 3d, Table 1).

To combine the influence of all the printing parameters, the volume-based energy density $E = \frac{P}{v \times h \times s}$ was used [22]. By fitting the power density dependence of the *DC* and Young's modulus (Fig. 3c), an empirical relationship was established as described by Eq. (2) to predict the mechanical properties of 2PP object produced with a given set of printing parameters.

$$E_{\text{PETA}} = 5.4 - \exp[f_0](3.4 - P/4vhs) \qquad (2)$$

We note that the relationship described by Eq. (2) is only valid for the structures produced with overlapping voxels ($h < d$, where *d* is the voxel diameter).

The effects of deposition parameters on the resolution [23], including the effect of laser power used on the voxel size [24,25] were reported and are known to determine the feature size and the surface roughness. The SEM and AFM images of woodpile blocks clearly showed an increase in surface roughness with increasing *h* (Fig. 4a-b). For a single printed line, the linewidth increased from ~200–450 μm when increasing *P* from 15 to 35 mW (Fig. 4c), which is proportional to an increase of the voxel diameter. At a laser power of 15 mW, the line width was 0.195 μm, which is about half of the hatching distance ($h = 0.4$ μm), thus the adjacent lines appear separated, leading to a surface roughness $Ra \sim 69$ nm. At a laser power of 30 mW, the line width was 0.386 μm, comparable with the hatching distance (0.4 μm), consequently surface roughness is reduced to $Ra \sim 9.6$ nm. This clearly indicated that roughness (Fig. 4c-d, Table 1) was dependent on the size of the hatching distance and the laser powers. Samples fabricated using $h < 0.4$ μm low roughness $Ra < 8$ nm was observed ($P = 22.5$ mW). For structures produced with larger $h \geq 0.5$ μm, surface roughness increased and a clear separation between the printed lines was observed. For these *h*, the *Ra* increases from 54 nm for $h = 0.5$ μm to $Ra = 220$ nm for $h = 1$ μm. This difference in roughness was attributed to the overlap between the voxels, and for *h* corresponding to non-overlapping voxels, the *Ra* value was found to be comparable to the axial size of the voxel.

One downside of decreasing hatching/slicing distances, however, is that the fabrication time increases dramatically. For example, compared to using a hatching distance $h = 0.3$ μm, the estimated fabrication time for a solid ball (Ø 50 μm) and a buckyball (Ø 50 μm) using Nanoscribe DeScribe software at a scan speed of 10 mm/s is ~1.5 and 4-times

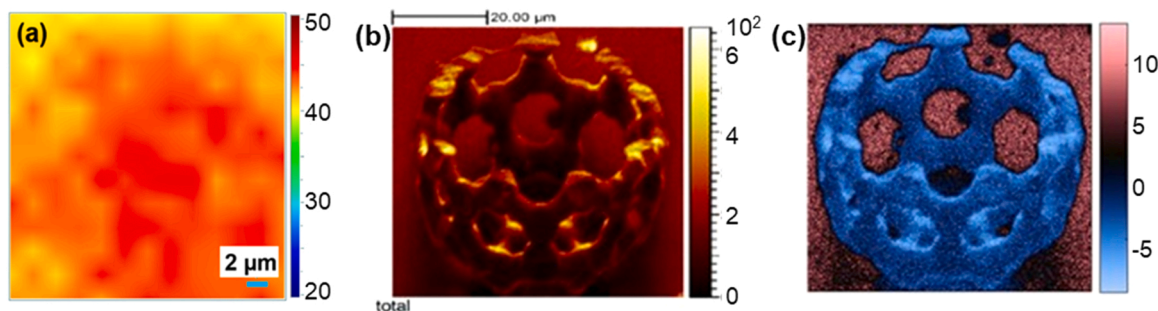**Fig. 2. (a)** Raman mapping image showing the uniformity of the degree of monomer consumption (*DC*) over an area of 25 μm x 25 μm of a 2PP cube. ToF-SIMS mapping images of total ion counts **(b)** and PCA scores **(c)** of a sectioned hollow sphere.
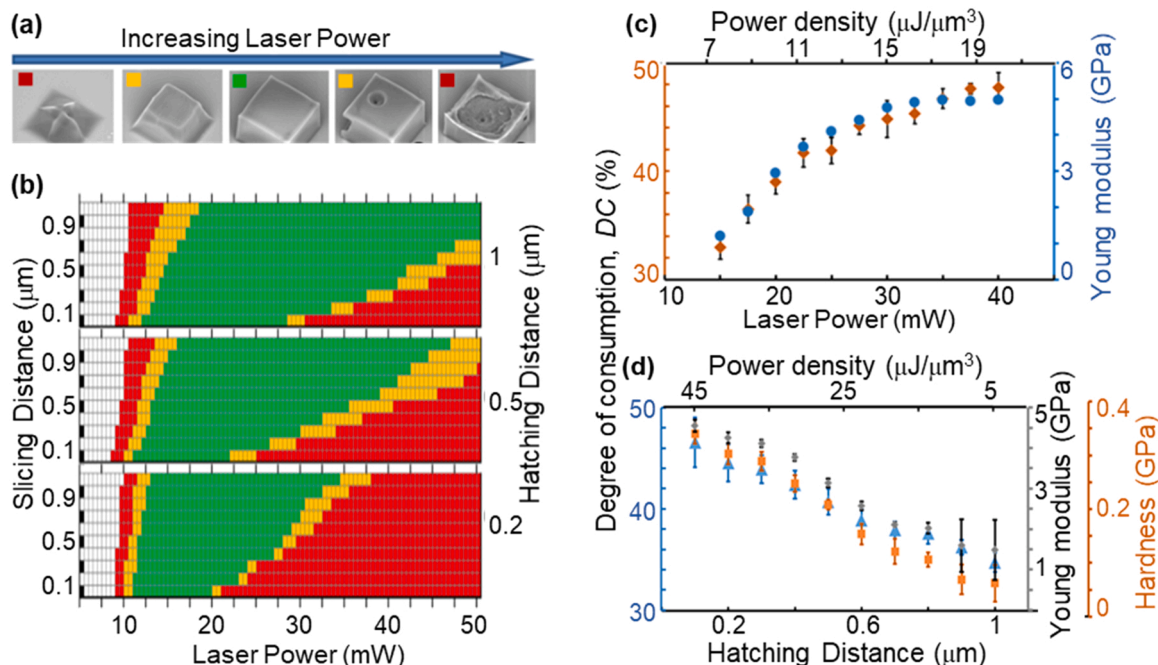
Fig. 3. (a) Representative scanning electron microscopy (SEM) images of 2PP cubes produced with PETA resin (0.18 mol% DETC). Processing parameters: $P = 22.5$ mW, $v = 10$ mm/s, $s = 0.5$ μm. **(b)** Processing windows are represented by assessment of the morphological properties: precise structure (green), minor morphological changes (yellow), unformed/burned (red) structures. Laser process window for $h = 1$, 0.5 and 0.2 μm and s in the range from 0.1 to 1 μm. $v = 10$ mm/ s. Dependence of the degree of consumption (DC) of vinyl groups on laser power **(c)** and hatching distance **(d)**. Dependence of Young modulus and hardness on laser power (c) and hatching distance (d).

Table 1
Summary of the effect of key 2PP parameters on the degree of consumption (DC), and morphological and mechanical properties for resin (0.18 mol% DETC).

2PP parameters			DC (%)	Morphological properties		Mechanical properties	
P (mW)	s (μm)	h (μm)		Line width (μm)	Roughness (nm)	Young modulus (Gpa)	Hardness (Gpa)
22.5	0.5	0.2	44		8	4.2	0.3
		0.4	42		15	3.6	0.25
		0.6	39		90	2.4	0.15
		0.8	37.5		180	1.8	0.1
		1	34		220	1.4	0.07
15	0.5	0.4	33	195	69	1.2	
22.5			42	260	15	3.8	
35			47	386	9.6	4.9	

longer, respectively, for $h = 0.2$ and 0.1 μm, respectively. Hence, the optimal printing parameters selected should achieve effective power density and voxel overlap in order to produce structures with uniform composition, smooth surface and required mechanical properties, within practical manufacturing times.

A commonly used strategy to optimize the relationship between the properties of the printed structure and the fabrication time is core-shell printing, where only the surface layers (shell) are printed with reduced hatching/slicing distances to achieve the smooth surface. Meanwhile, the interior (core) is printed with parameters set to achieve the required overall mechanical properties of the printed structure. Deformation and/or collapse may be observed after washing (see Supplementary Information SI3). However, this can be minimized by optimizing the thickness/spacing of the core structure. The presence of liquid resin trapped in the core might affect performance of the printed part, e.g. affecting the light propagation of an optical component, hence post-processing with UV exposure is used to solidify the trapped resin. For 3D structures with variable geometric slope, small (< 30 nm) or variable slicing distances, s, are used to achieve geometrical accuracy of the surface [26–28].

3.3. Sample transfer and multi-material printing

The knowledge developed above on the effect of printing parameters on the final properties of structures fabricated from individual monomers (Table 1) can be directly applied to produce 2PP multiple material structures. For each resin, we use optimised deposition parameters, which produced highest level of cure, as assessed by the DC value. We note that these DC values produce structures with mechanical properties that allow the fabricated structure to withstand washing cycles with no noticeable effect on its morphology. To fabricate multi-material structures, the multi-step strategy is used, where materials are sequentially loaded onto the substrate for 2PP with a washing step after the fabrication of an initial single material structure and prior to loading the second material (see experimental section for details).

There are three main challenges associated with step-by-step multi-material printing using 2PP: (i) alignment following substrate removal for washing [29]; (ii) a decrease in effective laser power, as light must propagate through multiple materials with different refractive indexes, hence the laser power used for each subsequent level needs to be increased to compensate for associated power losses; (iii) shrinkage, where fabrication of each material should ensure bonding to the existing
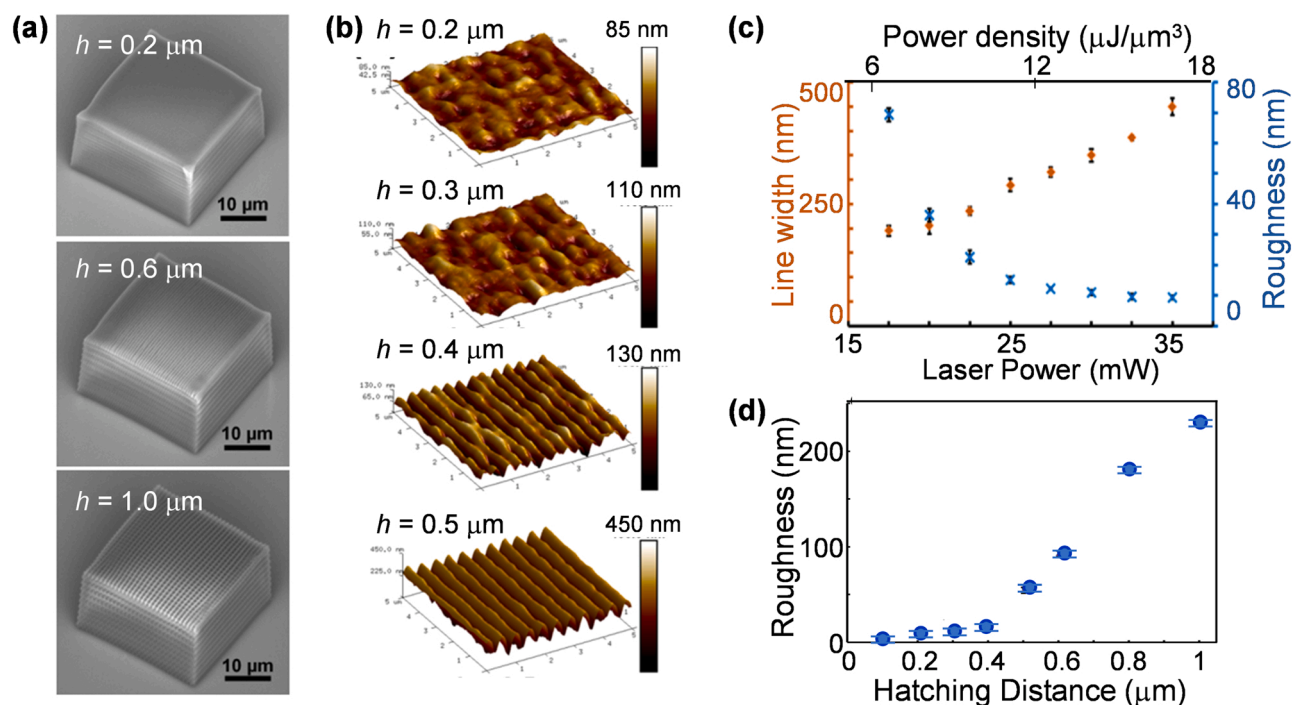
Fig. 4. Representative **(a)** SEM and **(b)** AFM images of woodpile 2PP blocks produced using PETA resin (0.18 mol% DETC) with different hatching distances, h. Dependence of linewidth and surface roughness on laser power (h = 0.4 mm, v = 10 mm/s) **(c)** and hatching distance (P = 22.5 W) **(d)**.

part, thus material shrinkage due to polymerisation must be taken into account (see Supplementary Information, SI3). Fig. 5a-c show the step-by-step 2PP process to fabricate a multi-material structure: a mat (TCDMDA, 0.2% PETA) with a basket (PETA, 0.2% PETA) filled with a sphere (PEGDA, 1.5% Irgacure369). Deformation and potential collapse of the multiphoton produced three-dimensional structures is one of the

major concerns in the field [30]. In our work, optimised printing parameters result in mechanical properties of the materials that preserve the integrity of the fabricated structures after each washing cycle. Optimized printing parameters allowed us to overcome the limitation of mixing dissimilar materials and offers opportunities for precise fabrication of multi-material 3D structures, with potential to combined
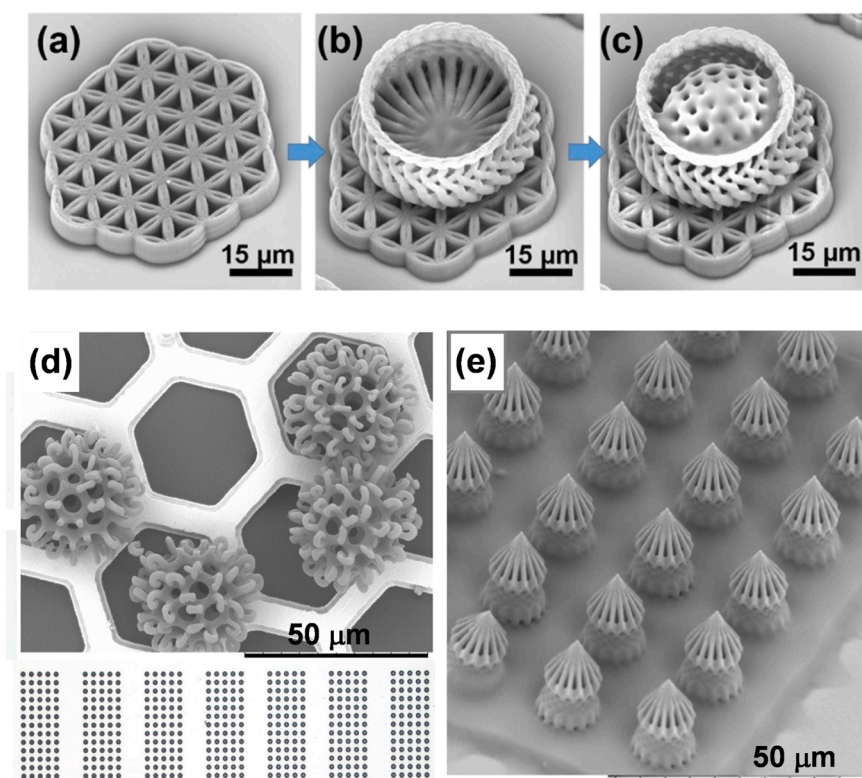

Fig. 5. Representative SEM images of structures produced in step-by-step multi-material 2PP fabrication. The TCDMDA mat **(a)** with PETA basket **(b)** and PEGDA (Mn700) ball **(c)**. DETC initiator was used for all monomers. **(d)** Optical images showing the successful removal of 454 out of 455 balls from a glass substrate; SEM image of hooked balls transferred onto a TEM grid from glass substrate (inset) on which array of hooked balls was printed. **(e)** An SEM image of PETA structures on a flexible substrate (Kapton; elongation at break: 250% tensile strength: 5 MPa).

materials with complementary mechanical, physical and chemical properties.

2PP structures are bound to the glass substrate for printing to ensure alignment and precision of printed parts. Yet, to enable realistic applications of these structures, their removal from the substrate is needed for transfer into a solution suitable for biomedical application and to realise precise assembly on a substrate [31] for integration into micro- and nano-scale device architectures [32,33]. To modify the strength of bonding to the substrate, the surface was pre-treated by chemical washing, plasma etching and silanization, and the laser focus during printing of the first layer was varied (0.5–1 μm into the substrate). We achieved optimised bonding strength by pre-treatment of glass substrate with IPA and silanization, and fabrication of first layer with laser focus 0.3 μm below the resin-glass interface. After 2PP, the samples were washed and sonicated for 15 s. Successful removal of 455 PETA balls from glass substrate and their transfer onto a TEM grid was achieved using this strategy (Fig. 5d). The 2PP structures removed from the substrate can be also dispersed in solution. Using the optimised parameters established here, it was possible to successfully fabricate PETA structures on a flexible Kapton substrate (Fig. 5e). The high fidelity and complex multi-materials structures demonstrated in our work are robust enough to sustain a multistep fabrication process and transfer onto a different substrate and/or into solution. This opens up exciting prospects for integration of these structures with materials/devices produced using conventional manufacturing as well as developing them for applications ranging from drug delivery to metamaterials, photonics and flexible electronics.

4. Conclusions

We established a systematic dependence of the effect of printing parameters on the degree of monomer consumption in 2PP structures for a number of monomer-initiator pairs. An empirical relationship between printing parameters and final properties of the 2PP structures was used to preselect the printing strategy to achieve desired properties from the final article. This predictive strategy was extended to the successful fabrication of complex architectures, including multi-material architectures with uniform composition, high spatial resolution, optimised mechanical properties and structural stability. This relationship was based on effective power density and was validated for printed structures, where the hatching distance is lower that the laser beam waist (i.e. there is a voxel overlap). Further work on development of a theoretical model to account for light-matter interaction within the individual voxel and for overlapping voxels is underway, as are attempts to include the effect of diffusion, steric hindrance, and chemical structure of monomers on *DC*. The results reported here are relevant for the development of additive manufacturing processes for high-resolution deposition of functional multi-materials.

CRediT authorship contribution statement

QH: Investigation, Methodology, Writing – Original Draft, **GR**: Investigation, Methodology **GFT**: Investigation, Methodology, **DP**: Investigation, Methodology, **LJ**: Investigation, Methodology, **AF**: Investigation, Methodology, **DI**: Conceptualization, Funding Acquisition **CT**: Conceptualization, Funding Acquisition, **RH**: Conceptualization, Funding Acquisition **RDW**: Conceptualization, Funding Acquisition, Writing – Review & Editing, **LT**: Writing – Review & Editing, Formal analysis.

Declaration of Competing Interest

The authors declare that they have no known competing financial interests or personal relationships that could have appeared to influence the work reported in this paper.

Appendix A. Supporting information

Supplementary data associated with this article can be found in the online version at doi:10.1016/j.addma.2021.102575.

References

[1] M. Carlotti, V. Mattoli, Functional Materials for Two-Photon Polymerization in Microfabrication, Small 15 (40) (2019), 1902687.
[2] Q. Hu, X.-Z. Sun, C.D.J. Parmenter, M.W. Fay, E.F. Smith, G.A. Rance, Y. He, F. Zhang, Y. Liu, D. Irvine, C. Tuck, R. Hague, R. Wildman, Additive manufacture of complex 3D Au-containing nanocomposites by simultaneous two-photon polymerisation and photoreduction, Sci. Rep. 7 (1) (2017) 17150.
[3] S.K. Saha, B. Au, J.S. Oakdale, High-Speed Direct Laser Writing of Silver Nanostructures via Two-Photon Reduction, Adv. Eng. Mater. 21 (9) (2019), 1900583.
[4] B. Buchegger, C. Vidal, J. Neuwirth, B. Buchroithner, A. Karner, A. Hochreiner, T. A. Klar, J. Jacak, Gold Nanoislands Grown on Multiphoton Polymerized Structures as Substrate for Enzymatic Reactions, ACS Mater. Lett. 1 (4) (2019) 399–403.
[5] A. Camposeo, L. Persano, M. Farsari, D. Pisignano, Additive Manufacturing: Applications and Directions in Photonics and Optoelectronics, Adv. Opt. Mater. 7 (2019) 25.
[6] G. Merkininkaitė, D. Gailevičius, S. Šakirzanovas, L. Jonušauskas, Polymers for Regenerative Medicine Structures Made via Multiphoton 3D Lithography, Int. J. Polym. Sci. 3403548 (2019).
[7] F. Hao, Z. Liu, M. Zhang, J. Liu, S. Zhang, J. Wu, H. Zhou, Y. Tian, Four new two-photon polymerization initiators with varying donor and conjugated bridge: Synthesis and two-photon activity, Spectrochim. Acta A 118 (2014) 538–542.
[8] Z. Li, A. Rosspeintner, P. Hu, G. Zhu, Y. Hu, X. Xiong, R. Peng, M. Wang, X. Liu, R. Liu, Silyl-based initiators for two-photon polymerization: from facile synthesis to quantitative structure–activity relationship analysis, Polym. Chem. 8 (43) (2017) 6644–6653.
[9] A.-I. Bunea, M.H. Jakobsen, E. Engay, A.R. Bañas, J. Glückstad, Optimization of 3D-printed microstructures for investigating the properties of the mucus biobarrier, Micro Nano Eng. 2 (2019) 41–47.
[10] Y. Liu, H. Wang, J. Ho, R.C. Ng, R.J.H. Ng, V.H. Hall-Chen, E.H.H. Koay, Z. Dong, H. Liu, C.-W. Qiu, J.R. Greer, J.K.W. Yang, Structural color three-dimensional printing by shrinking photonic crystals, Nat. Commun. 10 (1) (2019) 4340.
[11] K.S. Worthington, L.A. Wiley, E.E. Kaalberg, M.M. Collins, R.F. Mullins, E.M. Stone, B.A. Tucker, Two-photon polymerization for production of human iPSC-derived retinal cell grafts, Acta Biomater. 55 (Supplement C) (2017) 385–395.
[12] Q. Geng, D. Wang, P. Chen, S.-C. Chen, Ultrafast multi-focus 3-D nano-fabrication based on two-photon polymerization, Nat. Commun. 10 (2019) 2179.
[13] C.L. Lay, C.S.L. Koh, Y.H. Lee, G.C. Phan-Quang, H.Y.F. Sim, S.X. Leong, X. Han, I. Y. Phang, X.Y. Ling, Two-Photon-Assisted Polymerization and Reduction: Emerging Formulations and Applications, ACS Appl. Mater. Interfaces 12 (2020) 10061.
[14] A.J.G. Otuka, N.B. Tomazio, K.T. Paula, C.R. Mendonça, Two-Photon Polymerization: Functionalized Microstructures, Micro-Resonators, and Bio-Scaffolds, Polymers 13 (2021) 1994.
[15] G.F. Trindade, M.-L. Abel, J.F. Watts, Chemom. Intell. Lab. Syst. 182 (2018) 180–187.
[16] F. Zhang, Q. Hu, A. Castañon, Y. He, Y. Liu, B.T. Paul, C.J. Tuck, R.J.M. Hague, R. D. Wildman, Multi-branched benzylidene ketone based photoinitiators for multiphoton fabrication, Addit. Manuf. 16 (2017) 206–212.
[17] J. Fischer, J.B. Mueller, J. Kaschke, T.J.A. Wolf, A.N. Unterreiner, M. Wegener, Three-dimensional multi-photon direct laser writing with variable repetition rate, Opt. Express 21 (22) (2013) 26244–26260.
[18] J.B. Mueller, J. Fischer, F. Mayer, M. Kadic, M. Wegener, Polymerization Kinetics in Three-Dimensional Direct Laser Writing, Adv. Mater. 26 (38) (2014) 6566–6571.
[19] L.J. Jiang, Y.S. Zhou, W. Xiong, Y. Gao, X. Huang, L. Jiang, T. Baldacchini, J. F. Silvain, Y.F. Lu, Two-photon polymerization: investigation of chemical and mechanical properties of resins using Raman microspectroscopy, Opt. Lett. 39 (10) (2014) 3034–3037.
[20] T. Corrales, F. Catalina, C. Peinado, N.S. Allen, Free radical macrophotoinitiators: an overview on recent advances, J. Photochem. Photobiol. A 159 (2) (2003) 103–114.
[21] A. Eibel, D.E. Fast, G. Gescheidt, Choosing the ideal photoinitiator for free radical photopolymerizations: predictions based on simulations using established data, Polym. Chem. 9 (41) (2018) 5107–5115.
[22] L. Thijs, F. Verhaeghe, T. Craeghs, J.V. Humbeeck, J.-P. Kruth, A study of the microstructural evolution during selective laser melting of Ti–6Al–4V, Acta Mater. 58 (9) (2010) 3303–3312.

[23] S.-H. Park, D.-Y. Yang, K.-S. Lee, Two-photon stereolithography for realizing ultraprecise three-dimensional nano/microdevices, Laser Photon. Rev. 3 (1–2) (2009) 1–11.

[24] H.-B. Sun, K. Takada, M.-S. Kim, K.-S. Lee, S. Kawata, Scaling laws of voxels in two-photon photopolymerization nanofabrication, Appl. Phys. Lett. 83 (6) (2003) 1104–1106.

[25] X.Q. Zhou, Y.H. Hou, J.Q. Lin, A review on the processing accuracy of two-photon polymerization, AiP Adv. 5 (3) (2015).

[26] S.H. Park, S.H. Lee, D.Y. Yang, H.J. Kong, K.S. Lee, Subregional slicing method to increase three-dimensional nanofabrication efficiency in two-photon polymerization, Appl. Phys. Lett. 87 (15) (2005).

[27] X. Zheng, K. Cheng, X. Zhou, J. Lin, X. Jing, An adaptive direct slicing method based on tilted voxel of two-photon polymerization, Int. J. Adv. Manuf. Technol. 96 (2018) 521–530.

[28] X. Jing, K. Wang, J. Lin, P. Liu, Y. Kan, X. Zheng, J. Sun, Y. Li, Adaptive Slicing Method for Three-Dimensional Microstructures with Free-Form Surfaces in Two Photon Polymerization Microfabrication, Nano 14 (01) (2019), 1950006.

[29] F. Mayer, S. Richter, J. Westhauser, E. Blasco, C. Barner-Kowollik, M. Wegener, Multimaterial 3D laser microprinting using an integrated microfluidic system, Sci. Adv. 5 (2) (2019) eaau9160.

[30] S.-H. Park, K.H. Kim, T.W. Lim, D.-Y. Yang, K.-S. Lee, Investigation of three-dimensional pattern collapse owing to surface tension using an imperfection finite element model, Microelectron. Eng. 85 (2008) 432–439.

[31] S.-H. Park, Adaptive bonding technique for precise assembly of three-dimensional microstructures, Appl. Phys. Lett. 90 (2007), 233109.

[32] F. Qiu, R. Mhanna, L. Zhang, Y. Ding, S. Fujita, B.J. Nelson, Artificial bacterial flagella functionalized with temperature-sensitive liposomes for controlled release, Sens. Actuators B: Chem. 196 (2014) 676–681.

[33] R. Di Giacomo, S. Krödel, B. Maresca, P. Benzoni, R. Rusconi, R. Stocker, C. Daraio, Deployable micro-traps to sequester motile bacteria, Sci. Rep. 7 (2017) 45897.